



This document is published at :

Garg, S. K., Cuerno, R., Kanjilal, D. y Som, T. (2016). Anomalous behavior in temporal evolution of ripple wavelength under medium energy Ar⁺-ion bombardment on Si: A case of initial wavelength selection. *Journal of Applied Physics*, 119(22). (225301).

DOI: <https://doi.org/10.1063/1.4953378>

Anomalous behavior in temporal evolution of ripple wavelength under medium energy Ar⁺-ion bombardment on Si: A case of initial wavelength selection

Sandeep Kumar Garg,^{1,2} Rodolfo Cuerno,³ Dinakar Kanjilal,² and Tapobrata Som^{1,a)}

¹*Institute of Physics, Sachivalaya Marg, Bhubaneswar 751 005, India*

²*Inter-University Accelerator Centre, Aruna Asaf Ali Marg, New Delhi 110 067, India*

³*Departamento de Matematicas and Grupo Interdisciplinar de Sistemas Complejos (GISC), Universidad Carlos III de Madrid, 28911 Leganes, Spain*

(Received 8 February 2016; accepted 24 May 2016; published online 8 June 2016)

We have studied the early stage dynamics of ripple patterns on Si surfaces, in the fluence range of $1\text{--}3 \times 10^{18}$ ions cm^{-2} , as induced by medium energy Ar⁺-ion irradiation at room temperature. Under our experimental conditions, the ripple evolution is found to be in the linear regime, while a clear decreasing trend in the ripple wavelength is observed up to a certain time (fluence). Numerical simulations of a continuum model of ion-sputtered surfaces suggest that this anomalous behavior is due to the relaxation of the surface features of the experimental pristine surface during the initial stage of pattern formation. The observation of this hitherto unobserved behavior of the ripple wavelength seems to have been enabled by the use of medium energy ions, where the ripple wavelengths are found to be order(s) of magnitude larger than those at lower ion energies. *Published by AIP Publishing.* [<http://dx.doi.org/10.1063/1.4953378>]

I. INTRODUCTION

Spontaneous pattern formation during surface processing is one route to generate useful nanoscale textured materials.^{1–3} Ion-beam induced erosion of solids plays a major role to form self-organized surface nanopatterns in the form of ripples, dots, and faceted structures.^{4,5} It is a single-step process which is considered to be faster as compared to the conventional lithographic techniques, in order to create nanoscale patterns over large areas. Recently, ion-bombardment-induced surface corrugations have been shown to offer the potential to use them as substrates for deposition of nanofunctional thin films.^{6–8} To generate patterns, a target is exposed to a beam of energetic ions (typical energies in the range of hundreds of eV (Refs. 1 and 9) to tens of keV (Refs. 10–13,15) range) that impinge at a well-defined angle of incidence. Pattern formation under energetic ion bombardment is known to be governed by a number of parameters, such as ion-energy,¹⁴ -flux, -fluence, and -incidence angle.⁵ Moreover, despite having the similar experimental conditions, dissimilar surface morphologies are induced by ion beams, originating from different ion sources used in different laboratories.^{16,17} This shows that various experimental set ups and/or conditions at different research laboratories do play a role towards pattern formation.⁵

An important step to understand the cause of pattern formation was first put forward in the form of Bradley–Harper (BH) theory.¹⁸ This is a continuum model in which Sigmund's sputter erosion theory¹⁹ is combined with thermal surface diffusion²⁰ and studied through linear stability analysis. Indeed, quite generically, this type of analytical approximation suffices to characterize the onset of the

morphological instability responsible for pattern formation in many non-equilibrium systems.²¹ According to BH theory, the pattern formation under ion-beam irradiation occurs as a balance between two microscopic processes, viz., one that smoothens the surface (thermal surface diffusion) and another one that increases the surface roughness (removing surface atoms by ion-induced sputtering). However, the behavior of the ripple topography in many experimental observations cannot be explained by BH theory. In particular, both for low⁹ and for medium^{10,22} ion energy irradiation of silicon, ripple formation only occurs for ion incidence angle, θ , above a non-zero threshold value, θ_c (relatively close to 45°), while BH theory predicts pattern formation under any off-normal incidence angle. Carter and Vishnyakov¹⁰ (CV) were able to account for a non-zero value of θ_c by considering momentum transfer from the ions to the target atoms, also within a linear approximation. More recently, the CV mechanism has been reformulated as stress-induced viscous flow^{23,24} or as material redistribution,^{25–29} based on the surface amorphization that occurs on semiconductor surfaces under the present type of irradiation.

In the recent process or reassessment of the BH paradigm, most efforts have been directed to the early stages of evolution, which are controlled by linear effects. For the case of Si at low ion energies, it has been possible to assess experimentally important features of an underlying theoretical description, such as the morphological phase diagram in terms of ion energy and incidence angle.³⁰ Also the fact that the linear terms in the evolution equation for the surface topography have the same form (linear dispersion relation) as in BH theory, if possibly with a different interpretation.¹⁶

However, additional information on the early stage of pattern formation has been hard to obtain because of the inherent length scale associated with ripple wavelengths

^{a)}Author to whom correspondence should be addressed. Electronic mail: tsom@iopb.res.in

formed at low energies (up to a few keV). For instance, low-energy ions lead to evolution of ripples with wavelengths typically in the range of 20–50 nm.^{4,17,30–32} Thus, measurement of corresponding changes in wavelength due to a small variation in fluence at lower values (i.e., the early stage of ripple formation) becomes limited by the accuracy of the characterization tool and/or the associated error.¹⁶ As a result, initial wavelength of ripples (up to certain fluence) was reported to be constant (within the experimental resolution).^{31,33} Note that this is a non-trivial aspect because, within linear theory, the evolution of the surface height arises from a dynamical competition among Fourier modes of the surface topography corresponding to different wave-vectors (wavelength selection), the one with the fastest growth-rate setting the ripple wavelength.^{18,23} On general grounds, one would expect that the shape of the pristine surface may play a role in this competition, as has actually been assessed experimentally for related systems.^{32,34,35}

The behavior of silicon surfaces under low (up to 2 keV) and intermediate (up to 60 keV) energy ion bombardment has some commonalities. For instance, the absence of any pattern over the angular window of $0 < \theta < 45^\circ$ and the evolution of the ripple pattern at angles higher than 45° are similar for both regimes.^{4,9,12,36} However, ripple wavelengths at intermediate energies have much higher values (in the range of 700–1000 nm) compared to those formed at low energies.^{36,37} Such higher values of the ripple wavelength at intermediate energies should remove the inherent limitation of addressing small changes in low-energy ion-induced ripple wavelength at lower fluences (as discussed above), albeit determination of ripple wavelengths at lower energies using advanced characterization tools has been demonstrated efficiently.¹⁶ Therefore, for a better understanding of pattern formation at an early stage, intermediate energy keV ions can be an attractive tool.

In this paper, we report on the nature of wavelength selection for early stage of ripple formation on silicon surfaces due to 60 keV Ar⁺-ions. Experimental observations reveal a decreasing trend in ripple wavelength up to a certain time, which is compared with the linear stability analysis results based on continuum theories.

II. EXPERIMENTAL

In order to study the temporal evolution of the morphology of Si surfaces, commercially available *p*-type Si (100) samples of size $5 \times 5 \text{ mm}^2$ (*rms* roughness of 0.2 nm) were exposed to 60 keV Ar⁺-ions at room temperature (RT) at an incidence angle of 60° with respect to the surface normal. Prior to loading into the experimental chamber, the samples were ultrasonicated (in 10 min step) in trichloroethylene, isopropyl alcohol, acetone, and de-ionized water and, subsequently, placed in front of dry nitrogen. Several fluences in the range of 2×10^{17} to 3×10^{18} ions cm^{-2} were used, corresponding to a current density of $20 \mu\text{A cm}^{-2}$. All implantations were carried out under the secondary-electron-suppressed geometry, while the samples were mounted on a thick copper block using copper tapes. An electron cyclotron resonance (ECR) ion source was used to carry out this work.

Uniform irradiation was achieved by scanning the beam over the samples. A low-impurity environment was ensured during all implantations. Evolution of irradiation induced surface morphology was studied by *ex-situ* atomic force microscopy (AFM) in the ACTM mode (MFP3D, Asylum Research). A large number of AFM images were acquired for different scan areas (of 1×1 to $40 \times 40 \mu\text{m}^2$) and from different places to test the uniformity of patterns and to achieve high reliability of the extracted parameters.

III. RESULTS AND DISCUSSION

Figures 1(a)–1(d) and Figures S1(a)–S1(b)³⁸ show AFM images of Si samples before and after exposure to Ar⁺ ions. The arrow marks indicate the projection of the ion-beam direction onto the surface (identified as *x*-direction herein-after). The corresponding autocorrelation images and the respective line profiles are shown in the insets—at the right bottom corner of the corresponding images. AFM images of samples implanted below the fluence of 1×10^{18} ions cm^{-2} are not presented since they show uncorrelated rough surfaces. Thus, we may infer that ripples evolving at this fluence (1×10^{18} ions cm^{-2}) are at their very initial stages of formation. Autocorrelation images, rms surface roughness, and ripple height were extracted using the WSxM software.³⁹ Line profiles extracted from the respective autocorrelation images are used to calculate ripple wavelengths at different fluences. The calculated ripple wavelengths are found to be 900 ± 30 nm, 878 ± 22 nm, 850 ± 25 nm, 791 ± 28 nm, and 760 ± 20 nm for fluences of 1×10^{18} , 1.5×10^{18} , 2×10^{18} , 2.5×10^{18} , and 3×10^{18} ions cm^{-2} , respectively. Thus, we observe a clear decreasing trend in ripple wavelength with increasing irradiation time, somehow opposite to the pattern coarsening behavior with increasing fluence found at large irradiation times.¹³ In Fig. 1(e), we show 1D power spectral densities (PSD) extracted from the surface morphologies in Figs. 1(b)–1(d) and Figs. S1(a)–S1(b)³⁸ in the radial direction. The observed decreasing trend of ripple wavelength with increasing irradiation time is reflected in the position of the main peak in the PSD (dominant wavelength in the corresponding morphology) which is observed to shift towards higher values of *q* (here, $q = 2\pi/\text{ripple wavelength}$) [indicated by the vertical line in Fig. 1(e)].

It is known that the threshold fluences, flux, and the critical angle for pattern evolution on silicon surfaces are not unique at both low and intermediate energies.^{4,9,13,22,40} For instance, the results in the present study differ from the previous studies^{13,22,36} which were obtained under nearly similar experimental conditions. Likewise, in the present case, we get to see ripple patterns on crystalline Si surface at the fluence 1×10^{18} ions cm^{-2} ,^{22,36} while there are reports⁴¹ at comparable energies, where ripple patterns are observed at even lower fluences on pre-amorphized Si surfaces. In another work, Chini *et al.* observed that the wavelength and amplitude of Si ripples, evolved under comparable experimental conditions, can vary depending upon the beam scan rate.³⁷ In fact, over an energy range of 50–140 keV, they observed a smaller wavelength of ripples for irradiation without any beam scanning, which was attributed to

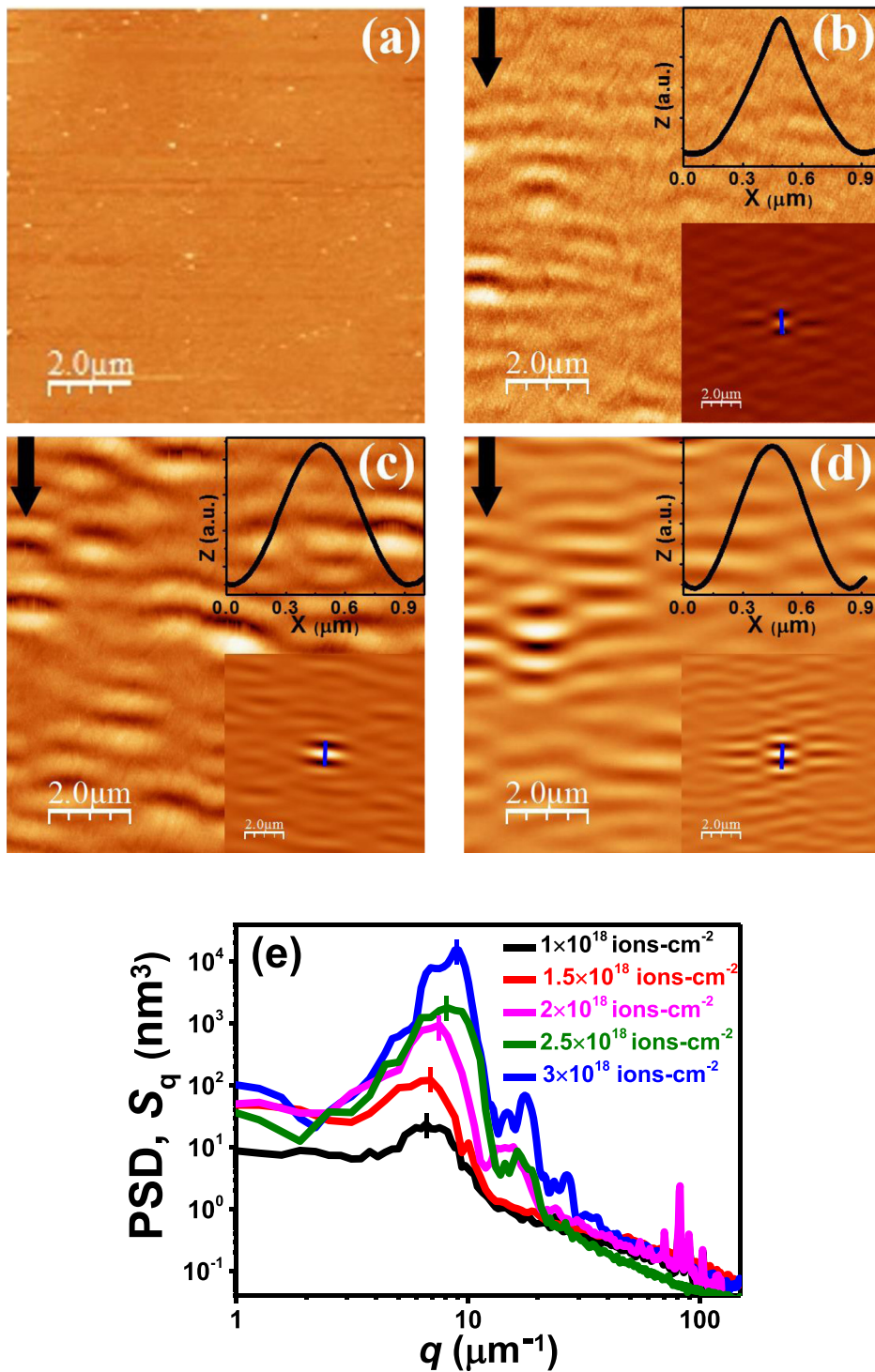


FIG. 1. AFM images ($10 \times 10 \mu\text{m}^2$) of Si samples before and after exposure to Ar^+ -ions at an incidence angle of $\theta = 60^\circ$: (a) Pristine Si surface; (b)–(d) implanted Si surfaces at the fluences 1×10^{18} , 2×10^{18} , and 3×10^{18} ions cm^{-2} , with height scales 4.0, 15.9, and 45.4 nm, respectively. The autocorrelation image and its line profile of the implanted samples are also shown as insets of the corresponding image. To maintain the clarity, selective AFM images, obtained from Ar-ion exposed samples, are presented here. Arrows indicate the direction of the incident ion-beam on the surfaces. (e) Radial 1D PSD calculated as a function of irradiation time. The vertical short line at the highest data point of each plot represents the characteristic wavelength of ripple pattern.

ion-induced heating and the resultant local temperature rise on the sample surface, originating from the nature of thermal contact of the Si sample with the copper sample-holder.³⁷ This result indicates that ripple dimensions evolved in a particular experimental situation are finally determined by specific conditions like surface temperature of the sample and, therefore, can vary even if external experimental parameters such as ion-energy, -fluence, or -angle of incidence remained the same. It may be mentioned that the scan rates are quite different⁴² in the present case compared to those mentioned in Refs. 13 and 37, which may also lead to such contrasting ripple dimensions, albeit the role of beam

scanning has not yet been defined in an explicit manner. Further to this, as discussed earlier, different ion sources are also known to lead to different ripple parameters, which are reported in numerous studies based on low energy Ar-ion induced pattern formation on the Si surface.^{13,16,17,22,31,32} In the same note, in the present study, the authors have used a different ion source compared to the one used in Refs. 13 and 37, which may as well lead to the observed difference in the ripple wavelengths evolving at an early stage.

In order to understand the anomalous behavior in terms of evolution of the ripple wavelength, we now go on to analyze additional surface features, namely, the shape and

amplitude of the ripples. For instance, we consider the distribution, $P(\gamma)$, of slope angles γ of the ripples by plotting a histogram of derivatives of the height profiles, which is shown in Fig. 2(a) for different values of the ion fluence. For the pristine sample, the distribution has a nominal width which is typical of a smooth surface. For argon-ion implanted samples, the peak position of the $P(\gamma)$ distribution represents the average slope of the ripples, where positive γ corresponds to the upstream side (front slope) of the ripples, facing the ion beam, and negative γ refers to the downstream side (rear slope) of the ripples. The symmetric distribution [Fig. 2(a)] around 0° indicates the similar shapes of the front and the rear slopes, which persists with increasing ion fluence. This symmetric peak at the gradient angle 0° is completely different from the asymmetric one which is reported in Refs. 22 and 43 for higher fluences, clearly revealing the symmetric nature of ripples. The widths of the distributions

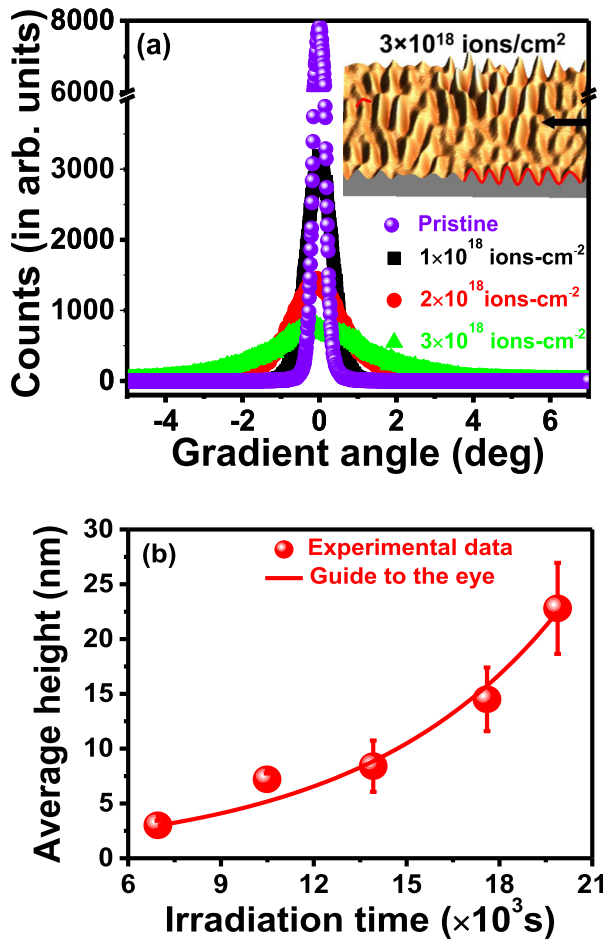


FIG. 2. (a) Selective gradient angle distributions of ripple patterns are shown for different fluences, along with the value for the pristine sample. To maintain the clarity, data for the two intermediate fluences have not been presented. Data for these plots were extracted from Fig. 1. For direct visualization of the ripple shape, the inset shows a three-dimensional AFM image of the irradiated sample corresponding to the highest fluence. Here, two solid lines are drawn on the image—one line follows the shape of the ripples at one edge of the image, while the other one follows the pattern in the middle of the image, showing the symmetric shape of the ripples. (b) Variation in the average ripple height with respect to Ar^+ -ion fluence (irradiation time). Error bars on the data points indicate the corresponding values of the roughness. The dotted line is a guide to the eye and corresponds to exponential increase.

corresponding to 1×10^{18} , 2×10^{18} , and 3×10^{18} ions cm^{-2} are 0.76° , 1.49° , and 2.67° , respectively, which indicates that the ripple height increases with fluence. This agrees well with our experimental observations, in which the average surface height (h), extracted from the AFM images, increases exponentially with ion fluence [Fig. 2(b)].

In order to understand the observed behavior, we now consider a continuum description of the system. Except perhaps for the time dependence of the ripple wavelength, all the observations (exponential increase of surface height, lateral symmetry of ripple shapes) suggest that, up to the largest fluence considered here, the system is within linear regime. In a reference frame which is moving with the average surface height, the evolution equation is then expected to read^{18,23}

$$\frac{\partial h(x, y)}{\partial t} \cong \nu_x \frac{\partial^2 h}{\partial x^2} + \nu_y \frac{\partial^2 h}{\partial y^2} - K \nabla^4 h + N[h] + \eta(x, y, t), \quad (1)$$

where ν_x , ν_y are the components of ion-induced “surface tension” (that may incorporate both BH-type erosive and CV-like surface-confined mass transport contributions), $-K \nabla^4 h$ accounts for surface relaxation processes (such as thermal surface diffusion and/or surface-confined viscous flow⁴⁴), $N[h]$ accounts for nonlinear corrections, henceforth assumed to be negligible, and $\eta(x, y, t)$ is Gaussian white noise with zero average and constant variance $2D$. This noise term accounts for the randomness of the microscopic processes going on (ion arrival, sputtering events, and surface diffusion attempts).⁴⁵ Actually, for low-energy Ar^+ -ion bombardment of clean Si targets, the linearized stochastic Eq. (1) has been explicitly demonstrated experimentally.¹⁶ Based on the strong similarities mentioned above between low- and medium-energy surface nanopatterning of Si, we will assume that Eq. (1) still provides an appropriate description of our medium-energy experiments. In particular, note that the form of the nonlinear terms, $N[h]$, remains an open issue in the field.

The linearized Eq. (1) can be readily solved by Fourier transform.^{18,23} Assuming a flat initial condition, each Fourier mode of the height evolves independently as $h_q \sim e^{r_q t}$, where $r_q = -(\nu_x q_x^2 + \nu_y q_y^2 + \kappa q^4)$, is the so-called linear dispersion relation and $\mathbf{q} = (q_x, q_y)$ is the wave-vector. Under pattern-forming conditions, the “surface-tension” coefficients, $\nu_{x,y} < 0$, so that r_q reaches a positive maximum for a given Fourier mode h_{q^*} . If one assumes that $\nu_x < \nu_y$ then $q^* = (|\nu_x|^{1/2} (2K)^{-1/2}, 0)$. Thus, the amplitude h_{q^*} dominates all other Fourier modes, leading to a ripple structure along the x -axis, with wavelength $\lambda = 2\pi/q^*$. This is the linear wavelength selection mentioned above. With respect to the time evolution, at very early times $t < t_{c1}$, Eq. (1) leads to a smoothing-like relaxation controlled by noise and the surface-diffusion like term.⁴⁶ At larger fluences $t_{c1} < t < t_{c2}$, one expects the development of the linear instability, during which exponential amplification of surface features (ripple amplitude and surface roughness) occurs. Finally, $t = t_{c2}$ signals the onset of nonlinear effects, once surface slopes have become sufficiently large. Typically, non-linear behavior is signaled by a slower rate (e.g., power-law) of increase for

the surface roughness, and sometimes additional effects such as wavelength coarsening, i.e., a power-law *increase* of the ripple wavelength with time.^{23,31}

Our experimental results show a hitherto unobserved *decreasing* trend in the ripple wavelength for the small values of the fluence which we study. For larger fluences, under our experimental conditions, non-linear effects are expected to occur.²² Thus, it is important to consider whether the time-dependent behavior that we obtain for the ripple wavelength can still be accounted for within the framework of Eq. (1). Thus far, the exponential growth in average ripple height with irradiation time that we observe indeed suggests that the temporal evolution of our ripple pattern is within the linear regime. To strengthen this conclusion further, we analyze the time-dependent shape evolution of the observed ripples, which can help to determine the transition from the linear to the non-linear regime. In fact, the correlation between the change in the ripple shape from a symmetric to an asymmetric one with the transition to the non-linear regime was put forward by Muñoz-García *et al.*,⁴⁷ subject to small-slopes condition, $h/\lambda \ll 1$. From Fig. 2(a), it is clear that the symmetric shape of the ripples persists for the fluence values under consideration, and in addition, the condition $h/\lambda \ll 1$ also holds true. These observations reinforce our working hypothesis that the temporal evolution of the ripple pattern in our experiment does belong to the linear regime $t_{c1} < t < t_{c2}$.

In order to fully describe the experimental behavior, we need to take into account the fact that the initial (pristine) surface is not mathematically flat; actually, it generically features non-trivial space correlations,³⁵ which may be particularly noticeable in the early-time evolution. Thus, in what follows, we perform numerical simulations of Eq. (1), in which the initial condition is the AFM image of the experimental pristine sample. This allows us to compare in detail the experimental observations with the dynamical evolution of the surface height according to the linear model. Indeed, in our simulations of Eq. (1), we have discarded the nonlinear terms $N[h]$. The values of the parameters ν_x , ν_y , K , and D were estimated from a fit of the structure factor $|h(\mathbf{q}, t)|^2$ for time t , obtained from the AFM images of the irradiated surface, in which its value at time $t=0$ (corresponding to the pristine surface) has been taken into account. Note that, for a non-flat initial condition with structure factor $|h(\mathbf{q}, 0)|^2$, the exact solution of Eq. (1) leads to^{16,48}

$$|h(\mathbf{q}, t)|^2 = \exp(2r_q t) \left(|h(\mathbf{q}, 0)|^2 + \frac{(2\pi)2D}{r_q} \right) - \frac{(2\pi)^2 D}{r_q}. \quad (2)$$

Using this equation, a simple-minded fit of the structure factors of samples irradiated for two different times, $t=6960$ s and 13920 s, provides $\nu_x = -5.18 \times 10^{-5} \mu\text{m}^2 \text{s}^{-1}$, $\nu_y = -2.4 \times 10^{-7} \mu\text{m}^2 \text{s}^{-1}$, $K = 4.16 \times 10^{-7} \mu\text{m}^4 \text{s}^{-1}$, and $D = 1.4 \times 10^{-12} \mu\text{m}^2 \text{s}^{-1}$. In our numerical simulations, we have employed periodic boundary conditions, a centered-differences discretization of Eq. (1), and an Euler–Maruyama scheme for the temporal evolution, with steps $\Delta x = \Delta y = 10/128 \mu\text{m}$, and $\Delta t = 2 \times 10^{-3}$ s, respectively. These choices of Δx and Δt allow direct comparison between simulated and experimentally

observed morphologies. We have confirmed that simulation results do not differ significantly for smaller step sizes. With the values of the parameters described above, the simulated surface morphologies are observed to correspond to the experimentally observed patterns (including consistent values of the ripple wavelength for each fluence) at irradiation times ten times smaller than those of the simulations. Given the uncertainty in estimating the value of t_{c1} (time of onset of the linear instability), and in order to reach a one-to-one correspondence between the simulation and the experimental results, we have scaled down the values of parameters ν_x , ν_y , and K uniformly by a factor of 10, thus keeping the wavelength of mode h_{q^*} unchanged, and the value of D by a factor of 3.

Surface morphologies, as simulated from Eq. (1), are shown in Figs. 3(a)–3(c) for simulation times 7000, 14 000, and 21 000 s, respectively. These three simulation times have been selected in order to reach an optimal correspondence between experimental and simulated morphologies. The simulation time 7000 s corresponds to an ion fluence of 1×10^{18} ions cm^{-2} , where ripple patterns start to appear. Simulation times 14 000 and 21 000 s are equivalent to ion fluences of 2×10^{18} and 3×10^{18} ions cm^{-2} , respectively.

In Fig. 3(d), we show power spectral densities (PSD) calculated for one-dimensional cuts of the surface morphologies in Figs. 3(a)–3(c) along the x -direction, parallel to the ripple wave-vector (vertical direction in the snapshots). In order to reduce the statistical fluctuations that can mask the position of local maxima, here, we choose to plot the 1D PSD instead of the 2D PSD. With increasing simulation time, the position of the main peak in the PSD (dominant wavelength in the corresponding morphology) is observed to shift towards higher values of q_x [indicated by the black line for each curve in Fig. 3(d)]. This implies a decreasing behavior of the ripple wavelength with increasing irradiation time. The average amplitude and wavelength of the simulated ripple patterns are plotted in Fig. 3(e). The error bars of the ripple amplitudes correspond to the roughness value (rms of the height distribution) for that simulated pattern. The wavelengths of the simulated ripple patterns in Fig. 3(e) are comparable with those of the experimentally observed ones described above at the respective sputtering times. Figure 3(e) also shows that the ripple amplitude (average height) increases exponentially, similarly to the experimental behavior [Fig. 2(a)]. Further quantitative differences between the simulated and the experimentally observed amplitude and roughness might be due to approximations involved in Eq. (1). Thus, we have only considered the terms that are most relevant to the evolution of the ripple amplitude and to the selection of the ripple wavelength, which have been experimentally motivated.^{16,31} In order to improve the quantitative description of the surface—and thus to account for additional features of the patterns, such as in-plane transport—additional terms are possibly required, such as third-order derivatives.⁴⁷

We should mention that the decreasing trend of the ripple wavelength with fluence does not occur in simulations when an ideally flat surface is employed as an initial condition ($t=0$), keeping the same set of parameter values as above [results not shown]. For example, in such case, the

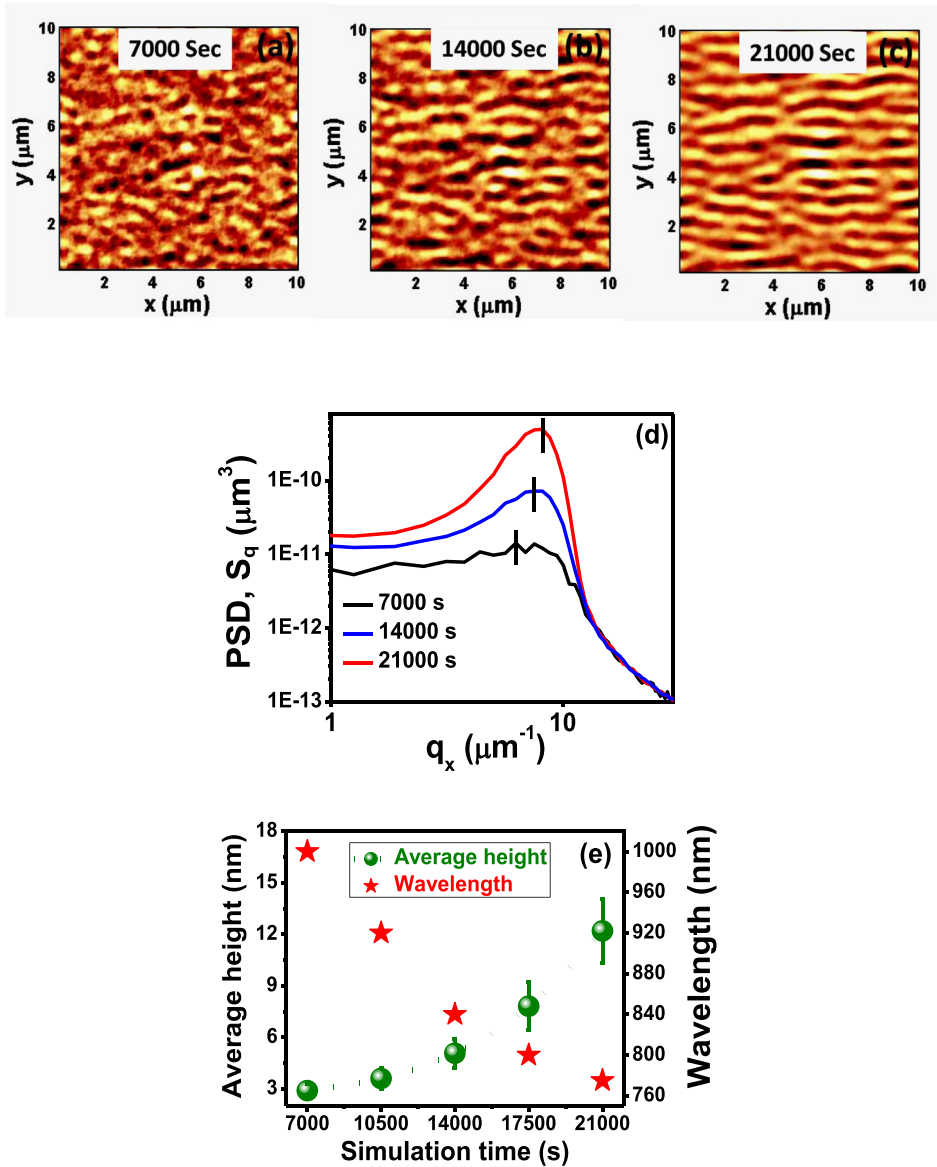


FIG. 3. Selective surface morphologies generated by numerical simulations. The images correspond to irradiation times (a) 7000, (b) 14000, and (c) 21000 s. (d) Corresponding power spectral densities, S_{q_x} . For each curve, the position of the absolute maximum is shown by a black line. (e) Average surface height and ripple wavelength as functions of irradiation time. As in Fig. 2, error bars shown for average heights indicate the corresponding values of the roughness.

ripple wavelength is found to remain constant with increasing simulation time. However, the ripple amplitude and roughness of the simulated morphology still have quite similar values at each simulation time as obtained for the pristine initial morphology.

Thus, our numerical simulations of Eq. (1) indicate that the decreasing behavior of the ripple wavelength with irradiation time, observed in the initial stage of pattern formation, is induced by the morphology of the initial surface. Intuitively, when Fourier-transformed, the form of the pristine surface turns out to have a relatively large contribution of long-wavelength (small q) modes h_q , which are less unstable than h_{q^*} . This implies that the maximum of the PSD takes place at a value of q_x which is smaller than q_{x^*} . The linear wavelength selection mechanism still holds, but it takes some time for the amplitude h_{q^*} to eventually dominate those of competing Fourier modes. Such a process is seen as a shift of the peak of the PSD towards the value corresponding to q_{x^*} . In real space, it is perceived as a decrease in the ripple wavelength with time. Naturally, different initial (pristine) conditions may lead to different behaviors from this point of

view. Moreover, the larger time and length scales associated with medium-energy irradiation as compared with low-energy experiments may justify the lack of reports of a similar behavior in the latter class of systems, for which the effect may be hard to resolve.

IV. CONCLUSIONS

Using 60 keV Ar^+ -ions at RT, we observe a decreasing trend in the ripple wavelength with ion fluence during the initial stages of the morphological evolution. To understand our results, we have carried out numerical simulations of a linear continuum model for ion irradiated surface evolution, having shown that the ripple evolution in our experiments is within a linear stage of evolution. Such a model has been assessed experimentally for Si irradiation at low ion energies. Comparison between the simulation and experimental results indicates that the time-dependent behavior of the ripple wavelength is due to the influence that the shape of the pristine surface has during the early stages of pattern formation. Although Eq. (1) is known to lead a time-independent

behavior of the ripple wavelength for the case of ideally flat initial conditions, it is likewise known to lead to time-dependent behavior in the presence of additional effects, such as conserved noise, which have also been assessed in experiments of interface dynamics at the nanoscale.⁴⁹ Thus, the shape of the initial condition appears as an additional ingredient for the design of patterns with desired morphological characteristics. In particular, the length scales associated with ripples formed at medium-energy ion irradiation can aid to obliterate the limitation to probe a variation in pattern dimension which is encountered in low-energy experiments.

ACKNOWLEDGMENTS

The authors are thankful to D. P. Datta from National Institute of Science Education and Research (NISER), Bhubaneswar, for his support and discussion at various stages of this work. R.C. acknowledges funding by MINECO (Spain) through Grant Nos. FIS2012-38866-C05-01 and FIS2015-66020-C2-1-P. S.K.G. acknowledges local support by Universidad Carlos III de Madrid during a short-term visit.

- ¹S. Facsko, T. Dekorsy, C. Koerdt, C. Trappe, H. Kurz, A. Vogt, and H. L. Hartnagel, *Science* **285**, 1551 (1999).
- ²V. Venugopal, S. K. Garg, T. Basu, O. P. Sinha, D. Kanjilal, S. R. Bhattacharyya, and T. Som, *Appl. Surf. Sci.* **258**, 4144 (2012).
- ³S. K. Garg, D. P. Datta, J. Ghatak, I. Thakur, K. Khare, D. Kanjilal, and T. Som, *RSC Adv.* **6**, 48550 (2016).
- ⁴T. Basu, J. R. Mohanty, and T. Som, *Appl. Surf. Sci.* **258**, 9944 (2012).
- ⁵T. Som and D. Kanjilal, *Nanofabrication by Ion-Beam Sputtering: Fundamentals and Applications* (Pan Stanford, Singapore, 2012).
- ⁶J. Fassbender, T. Strache, M. Liedke, D. Markó, S. Wintz, K. Lenz, A. Keller, S. Facsko, I. Mönch, and J. McCord, *New J. Phys.* **11**, 125002 (2009).
- ⁷M. O. Liedke, M. Körner, K. Lenz, M. Fritzsche, M. Ranjan, A. Keller, E. Čizmar, S. A. Zvyagin, S. Facsko, K. Potzger, J. Lindner, and J. Fassbender, *Phys. Rev. B* **87**, 024424 (2013); M. O. Liedke, M. Korner, K. Lenz, F. Grossmann, S. Facsko, and J. Fassbender, *Appl. Phys. Lett.* **100**, 242405 (2012).
- ⁸K. V. Sarathlal, D. Kumar, and A. Gupta, *Appl. Phys. Lett.* **98**, 123111 (2011).
- ⁹C. S. Madi, B. Davidovitch, H. B. George, S. A. Norris, M. P. Brenner, and M. J. Aziz, *Phys. Rev. Lett.* **101**, 246102 (2008).
- ¹⁰G. Carter and V. Vishnyakov, *Phys. Rev. B* **54**, 17647 (1996).
- ¹¹G. Carter, V. Vishnyakov, Y. V. Martynenko, and M. J. Nobes, *J. Appl. Phys.* **78**, 3559 (1995).
- ¹²G. Carter, V. Vishnyakov, and M. J. Nobes, *Nucl. Instrum. Methods Phys. Res. B* **115**, 440 (1996).
- ¹³D. P. Datta and T. K. Chini, *Phys. Rev. B* **69**, 235313 (2004).
- ¹⁴S. K. Garg, D. P. Datta, J. Ghatak, S. R. Tripathy, D. Kanjilal, and T. Som, *Appl. Surf. Sci.* **317**, 476 (2014).
- ¹⁵A. Biermanns, U. Pietsch, J. Grenzer, A. Hanisch, S. Facsko, G. Carbone, and T. H. Metzger, *J. Appl. Phys.* **104**, 044312 (2008).
- ¹⁶C. S. Madi, E. Anzenberg, K. F. Ludwig, Jr., and M. J. Aziz, *Phys. Rev. Lett.* **106**, 066101 (2011).
- ¹⁷T. Basu and T. Som, *Appl. Surf. Sci.* **310**, 142 (2014).
- ¹⁸R. M. Bradley and J. M. E. Harper, *J. Vac. Sci. Technol. A* **6**, 2390 (1988).

- ¹⁹P. Sigmund, *Phys. Rev.* **184**, 383 (1969).
- ²⁰W. W. Mullins, *J. Appl. Phys.* **28**, 333 (1957).
- ²¹M. Cross and H. Greenside, *Pattern Formation and Dynamics in Nonequilibrium systems* (Cambridge University Press, UK, 2009).
- ²²S. K. Garg, D. P. Datta, M. Kumar, D. Kanjilal, and T. Som, *Appl. Surf. Sci.* **310**, 147 (2014).
- ²³R. Cuerno, M. Castro, J. Muñoz-García, R. Gago, and L. Vázquez, *Nucl. Instrum. Methods Phys. Res. B* **269**, 894 (2011).
- ²⁴M. Castro and R. Cuerno, *Appl. Surf. Sci.* **258**, 4171 (2012).
- ²⁵S. A. Norris, J. Samela, L. Bukonte, M. Backman, F. Djurabekova, K. Nordlund, C. S. Madi, M. P. Brenner, and M. J. Aziz, *Nat. Commun.* **2**, 276 (2011).
- ²⁶M. Hossain, K. Das, J. Freund, and H. Johnson, *Appl. Phys. Lett.* **99**, 151913 (2011).
- ²⁷M. Moseler, P. Gumbsch, C. Casiraghi, A. C. Ferrari, and J. Robertson, *Science* **309**, 1545 (2005).
- ²⁸S. A. Norris, M. P. Brenner, and M. J. Aziz, *J. Phys.: Condens. Matter* **21**, 224017 (2009).
- ²⁹N. Kalyanasundaram, J. Freund, and H. Johnson, *J. Phys.: Condens. Matter* **21**, 224018 (2009).
- ³⁰C. S. Madi and M. J. Aziz, *Appl. Surf. Sci.* **258**, 4112 (2012).
- ³¹M. Castro, R. Gago, L. Vázquez, J. Muñoz-García, and R. Cuerno, *Phys. Rev. B* **86**, 214107 (2012).
- ³²A. Keller, R. Cuerno, S. Facsko, and W. Möller, *Phys. Rev. B* **79**, 115437 (2009).
- ³³J. Erlebacher, M. J. Aziz, E. Chason, M. B. Sinclair, and J. A. Floro, *Phys. Rev. Lett.* **82**, 2330 (1999).
- ³⁴J. Muñoz-García, R. Gago, L. Vázquez, J. A. Sanchez-García, and R. Cuerno, *Phys. Rev. Lett.* **104**, 026101 (2010).
- ³⁵J. Muñoz-García, R. Gago, R. Cuerno, J. A. Sánchez-García, A. Redondo-Cubero, M. Castro, and L. Vázquez, *J. Phys.: Condens. Matter* **24**, 375302 (2012).
- ³⁶S. K. Garg, V. Venugopal, T. Basu, O. P. Sinha, S. Rath, D. Kanjilal, and T. Som, *Appl. Surf. Sci.* **258**, 4135 (2012).
- ³⁷T. K. Chini, M. K. Sanyal, and S. R. Bhattacharyya, *Phys. Rev. B* **66**, 153404 (2002).
- ³⁸See supplementary material at <http://dx.doi.org/10.1063/1.4953378> for AFM images of irradiated Si at ion fluences of 1.5×10^{18} ions cm^{-2} and 2.5×10^{18} ions cm^{-2} .
- ³⁹See <http://www.nanotec.es/products/wsxm/> for Nanotec, *WSxM Software* The Nanotechnology Research Tool.
- ⁴⁰A. Moreno-Barrado, M. Castro, R. Gago, L. Vázquez, J. Muñoz-García, A. Redondo-Cubero, B. Galiana, C. Ballesteros, and R. Cuerno, *Phys. Rev. B* **91**, 155303 (2015).
- ⁴¹T. Kumar, A. Kumar, D. Agarwal, N. Lalla, and D. Kanjilal, *Nanoscale Res. Lett.* **8**, 336 (2013); T. Kumar, A. Kumar, and D. Kanjilal, *Appl. Phys. Lett.* **103**, 131604 (2013).
- ⁴²D. P. Datta, *Modification of Silicon Surface Under Medium Energy Heavy Ion Bombardment* (Saha Institute of Nuclear Physics, Kolkata, 2008).
- ⁴³S. K. Garg, D. P. Datta, T. Basu, D. Kanjilal, and T. Som, *Surf. Topogr.: Metrol. Prop.* **4**, 015002 (2016).
- ⁴⁴C. C. Umbach, R. L. Headrick, and K.-C. Chang, *Phys. Rev. Lett.* **87**, 246104 (2001).
- ⁴⁵M. A. Makeev, R. Cuerno, and A.-L. Barabási, *Nucl. Instrum. Methods Phys. Res. B* **197**, 185 (2002).
- ⁴⁶R. Cuerno, H. A. Makse, S. Tomassone, S. T. Harrington, and H. E. Stanley, *Phys. Rev. Lett.* **75**, 4464 (1995).
- ⁴⁷J. Muñoz-García, R. Cuerno, and M. Castro, *Phys. Rev. B* **78**, 205408 (2008).
- ⁴⁸T. Da Silva and J. Moreira, *Phys. Rev. E* **56**, 4880 (1997).
- ⁴⁹R. Fetzer, M. Rauscher, R. Seemann, K. Jacobs, and K. Mecke, *Phys. Rev. Lett.* **99**, 114503 (2007).